Articles

Spinning Disk Confocal Microscopy of Live, Intraerythrocytic Malarial Parasites. 1. Quantification of Hemozoin Development for Drug Sensitive versus Resistant Malaria†

Bojana Gligorijevic,‡ Ryan McAllister,§ Jeffrey S. Urbach,§ and Paul D. Roepe*,‡,||

Department of Chemistry, Department of Biochemistry and Molecular Biology, and Program in Tumor Biology, Lombardi Cancer Center, Department of Physics, and Center for Infectious Diseases, Georgetown University, 37th and O Streets, Washington, D.C. 20057

Received May 24, 2006; Revised Manuscript Received August 1, 2006

ABSTRACT: We have customized a Nipkow spinning disk confocal microscope (SDCM) to acquire three-dimensional (3D) versus time data for live, intraerythrocytic malarial parasites. Since live parasites wiggle within red blood cells, conventional laser scanning confocal microscopy produces blurred 3D images after reconstruction of *z* stack data. In contrast, since SDCM data sets at high *x*, *y*, and *z* resolution can be acquired in hundreds of milliseconds, key aspects of live parasite cellular biochemistry can be much better resolved on physiologically meaningful times scales. In this paper, we present the first 3D DIC transmittance "*z* stack" images of live malarial parasites and use those to quantify hemozoin (Hz) produced within the living parasite digestive vacuole, under physiologic conditions. Using live synchronized cultures and voxel analysis of sharpened DIC *z* stacks, we present the first quantitative in vivo analysis of the rate of Hz growth for chloroquine sensitive (CQS) versus resistant (CQR) malarial parasites. We present data for laboratory strains, as well as *pfcrt* transfectants expressing a CQR conferring mutant *pfcrt* gene. We also analyze the rate of Hz growth in the presence and absence of physiologically relevant doses of chloroquine (CQ) and verapamil (VPL) and thereby present the first in vivo quantification of key predictions from the well-known Fitch hypothesis for CQ pharmacology. In the following paper [Gligorijevic, B., et al. (2006) *Biochemistry 45*, pp 12411−12423], we acquire fluorescent images of live parasite DV via SDCM and use those to quantify DV volume for CQS versus CQR parasites.

Antimalarial drug resistance is a global tragedy of staggering proportions (*1*). New drugs that act on known targets and new targets for additional drug and vaccine development are urgently needed. Most conventional molecular methods are useful in meeting these goals, but many suffer from one or more drawbacks because *Plasmodium falciparum* malarial parasites are intracellular and are typically studied using relatively low density human blood culture, which is difficult and expensive. Gene transfection techniques that are dependent on blood culture have improved markedly in recent years, yet many genes of interest remain somewhat inaccessible to routine manipulation within bulk parasite cultures. Heterologous expression of malarial proteins in more easily manipulated culture systems (e.g., yeast and bacteria) can be very difficult due to the high AT content of *P. falciparum* genes (*2*). Also, the very curious cell biology of the parasite yields many surprises, further necessitating specialized approaches to many questions.

Thus, many questions that are routine in other systems are quite difficult to resolve because *P. falciparum* is an intracellular parasite that is tediously grown as a low-density blood culture in the laboratory. The problem is even more acute in studying other *Plasmodium* species that infect humans, since these are even more difficult to culture (e.g., *Plasmodium vivax*, for which current culturing methods require the regular infusion of fresh human reticulocytes). To make more rapid progress, biophysical techniques with single-cell resolution are being adapted and developed for the study of living parasites. These typically require the capability to either visualize or experimentally traverse multiple cell membranes (i.e., red cell plasma membrane, parasite parasitophorous and plasma membranes, etc.). To study the subcellular physiology and biochemistry of the living organism in situ requires specialized cellular and molecular imaging approaches, as well as specialized perfusion conditions and other modified procedures. These are still in their infancy, but their further development is crucial because it is the unique subcellular physiology and biochem-

† Supported by NIH Grants AI56312 and AI45759 to P.D.R. and NSF Grant DBI 0353030 to J.S.U.

* To whom correspondence should be addressed. Telephone: (202) 687-7300. Fax: (202) 687-6209. E-mail: roepep@georgetown.edu.

‡ Department of Chemistry, Department of Biochemistry and Molecular Biology, and Program in Tumor Biology, Lombardi Cancer Center.

§ Department of Physics.

|| Center for Infectious Diseases.

10.1021/bi061033f CCC: $33.50
Published on Web 09/20/2006

istry of unique parasite organelles that is critical for their incredibly rapid growth within the red cell [e.g. the digestive vacuole (DV),[1] the apicoplast, and a single atypical mitochondrion] that arguably offers the best array of unique potential drug targets.

Thus, we and others have endeavored to develop customized single-cell imaging approaches for analyzing live malarial parasites within the human red cell, using conventional laser scanning confocal microscopy (LSCM) or single-cell photometry (SCP) techniques (e.g., refs *3*−*6*). These methods have provided important data about the ionic environment of the parasite digestive vacuole (DV), protein traffic to the parasite apicoplast, and parasite differentiation during the erythrocytic stage of the cell cycle, as well as other key concepts, yet because of parasite movement within the red cell, photobleaching constraints, and other issues, many questions can only be fully answered with full 3D data sets that are obtained at hundreds of milliseconds time resolution or better. SCP has the requisite time resolution but not 3D spatial resolution, and vice versa for LSCM. In theory, because up to 20 000 pinholes arranged in pinwheel fashion can be used and very rapidly accessed (vs one pinhole for LSCM), SDCM has the potential to satisfy both the time and spatial resolution challenges that prevent elucidation of key remaining questions.

For example, a major challenge in malaria research is elucidating the exact basis of quinoline molecular pharmacology in vivo. Amino quinoline drugs such as chloroquine (CQ) have been the mainstay of antimalarial therapy for decades, but resistance to these compounds continues to both spread and evolve. To fully understand drug resistance and to develop new drugs require that we better understand the true molecular pharmacology of these compounds. One popular theory for amino quinoline action, based primarily on a very large amount of in vitro data, is the Fitch hypothesis (*7*). To grow rapidly within the red cell, the parasite must rapidly digest hemoglobin (Hb) within the parasite digestive vacuole (DV) (*8*). The unmetabolized byproduct of this digestion, ferriprotophyrin IX (FPIX) heme, is detoxified not by a heme oxygenase enzymatic pathway but by crystallization to hemozoin (Hz; also known as malarial pigment) (*9*, *10*). Hz deposited in the DV harms the human host upon subsequent lysis of the infected red blood cell (iRBC) but is innocuous to the growing parasite. The Fitch hypothesis states that uncrystallized FPIX released during Hb digestion is the essential target for CQ and other quinoline drugs. Presumably, binding of these drugs to one or more forms of uncrystallized heme acts to build up toxic levels of FPIX or FPIX−drug conjugates which then exert directly deleterious effects and/or promote oxidative stress. In support of this idea, Hz formation in vitro is indeed inhibited by CQ and other quinoline-based drugs, and reasonable correlations are found when plotting in vitro Hz formation IC_{50} values versus in vivo parasite toxicity (*11*). Also, several studies (e.g., refs *12*−*15*) have provided data that suggest CQ toxicity is maximal at either the trophozoite stage or the ring−trophozoite boundary, namely, the stages of parasite differentiation at which FPIX-to-Hz processing is maximal or begins, respectively. Finally, atomic resolution NMR data clearly show that CQ, QN, QD, and AQ form quite interesting noncovalent complexes with FPIX dimers (*16*, *17*) and that CQ can also form a covalent complex with monomeric FPIX (*18*). Taken together, the data suggest that these important antimalarial drugs inhibit Hz growth in vivo in some fashion, perhaps via a combination of chemical routes whose ratio would be highly drug specific.

However, the presumed overall effects on Hz formation have never been quantified in vivo; the exact nature of the in vivo effect(s) remains unknown, and quantitative comparison between presumed in vivo inhibition for CQS and CQR parasites has not been carried out. An attractive scenario based on data published to date is that inhibition of Hz growth in vivo by CQ might exhibit kinetic or dose dependency differences for CQS versus CQR parasites. These differences are key features of various models for the mechanism of CQR. In vivo, it is possible that CQ and related drugs either prevent formation of Hz by binding to one or more forms of FPIX, destabilize growing Hz by binding to one or more growing crystal faces (*9*, *10*), destablize preformed Hz, or carry out perhaps some combination. With regard to the later possibilities, these drugs could impede Hz crystallite formation, stall crystal nucleation, or have effects on higher-order processes. Distinguishing between these is crucial for ongoing structure-based quinoline drug design and for understanding new classes of antimalarials as they continue to emerge.

In this and the following paper (*19*), we describe a novel approach that will begin to resolve these issues via SDCM experiments with a highly synchronized *P. falciparum* blood culture followed by application of a two-step deblurring procedure and voxel analysis.

MATERIALS AND METHODS

Materials

All routine materials were reagent grade or better and purchased from commercial sources. Red blood cells and pooled human serum from anonymous donors were from Biochemed (Winchester, VA). DIC spherical size standards were purchased from Merck Chimie SAS (Pithiviers, France) and Bang Laboratories (Fishers, IN).

Methods

Cell Culture. P. falciparum CQR strains Dd2 and $C3^{Dd2}$ and CQS strains HB3 and GCO3 were grown in sealed flasks at 37 °C in a 5% CO_2/5% O_2/90% N_2 atmosphere (*20*). Frozen vials containing glycerolyte and seed culture at 4% parasitemia were thawed and maintained in flasks (Corning, 70 mL, plug seal) at 2% parasitemia in RPMI 1640 medium supplemented with 10% O+ human serum, 24.2 mM $NaHCO_3$, 5 mM glucose, 50 μg/L gentamycin, 25 mM HEPES (pH 7.4), and 0.1 mM hypoxanthine. Parasitemia was monitored, and the medium was changed every 48 h.

Synchronization. For this work, all cultures were routinely synchronized every three cycles with a 5% D-sorbitol

[1] Abbreviations: SDCM, spinning disk confocal microscopy; DIC, differential interference contrast; Hz, hemozoin; CQS, chloroquine sensitive; CQR, chloroquine resistant; CQ, chloroquine; VPL, verapamil; DV, digestive vacuole; LSCM, laser scanning confocal microscopy; SCP, single-cell photometry; FPIX, ferriprotoporphyrin IX; QN, quinine; QD, quinidine; AQ, amodiaquine; RBC, red blood cell; iRBC, malaria-infected red blood cell; 2D, two-dimensional; 3D, three-dimensional.

treatment (*21*) which lyses mid-stage and late trophozoites as well as schizonts but leaves uninfected RBC, rings, and some early trophozoites unscathed. In our hands, multiple synchronization treatments successively improve the ring: early trophozoite ratio, so we routinely synchronized three times. The first two treatments are in cell cycle 1, 4 and 14 h after the first visually observed RBC invasion event (most of the culture consists of schizonts). In this way, 0−4-hour-old rings are primarily left after the first synchronization, and lingering other stages are further eliminated at 14 h. The third treatment is 4 h after the first observed invasion in the following cell cycle. For the data presented in the Results, the time of the last synchronization step in cycle $x + 1$ is marked as time "0 h".

Spinning Disk Confocal Microscopy (SDCM). The starting point for our customized SDCM system is the 2003 model Perkin-Elmer UltraView SDCM device containing a Yokogawa CSU21 spinning disk confocal scan head and a Nikon TE 2000 inverted microscope with a 0.8 NA condenser and fitted with 1.4 NA 60× and 100× VC oil objectives. The microscope stage is a Merzhauser motorized XY translation stage with 0.02 μm accuracy and 0.25 μm repeatability, and the focus stepper is a Piezosystems jena objective piezoelectric controller. Important additions or custom modifications to the commercially available instrument include a Uniblitz high-speed shutter, a Hamamatsu ORCA ER cooled CCD camera, a Coherent Innova 300 Ar/Kr laser capable of 800 mW output power, and a NEOS acousto optic tunable filter (for fast illumination control). We have also fitted this system with customized Nikon DIC optics consisting of a linear polarizer, an analyzer, a condenser, and objective Nomarski prisms (all optimized for properties of the specific objective used) and custom cell perfusion chambers described elsewhere (*4*). In addition, the customized apparatus is mounted on a Newport Corp. pneumatic vibration isolation table to further minimize image blurring and other artifacts.

For 3D imaging of live cells, SDCM is able to achieve higher temporal resolution (frame rate) of cells relative to typical LSCM. In brief, this is because it uses at least 1000 pinholes at a time in conjunction with a CCD camera, rather than a single pinhole and a PMT. This allows faster collection of multiple images displaced along the *z* axis ("*z* slices"); thus, SDCM can therefore provide improved 3D reconstructions of moving organelles and particles by avoiding blurring caused by motion. The confocal head itself is able to scan 1000 frames per second (*22*). The rate of data transfer is essentially limited to camera speed and is currently similar to the video rate [approximately 30 frames (1000 × 1000 pixels)/s] but can in theory approach 1000 frames/s. The Nipkow spinning disk method is rotation of a disk with many holes arranged in a pinwheel fashion (*23*). Initially, multiple problems limited the utility of Nipkow disks in cellular optical microscopy. These included a low signal-to-noise ratio and inequality of light intensities in the inner and outer disk periphery. However, upgraded newer Nipkow disks (e.g., ref *24*) utilize arrays of up to 20 000 pinholes that are more equally spaced, along with a coordinated spinning coaxial pattern array of microlenses. For the data in this paper, importantly, fast *z* sectioning is enabled by a very high quality piezo-actuator attached to the objective lens. In sum, improved optics, shortened scanning times, and fast *z* axis displacement minimize illumination artifacts, photobleaching effects, and blurring; thus, a higher 3D resolution of fast moving particles (e.g., Hz in wiggling intraerythrocytic parasites) is made possible. For example, we can acquire a sufficient number of optical sections to reconstruct a living malarial parasite cell within the parasitized red blood cell at better than 250 nm resolution (*x*, *y*, and *z*) in ≤800 ms. The *xy* resolution of these SDCM data is only slightly lower than that of classical LSCM confocal data (measured on our instrument to be 213 nm using 500 nm light; see also ref *25*). Finally, the confocal image is observed in real time so it can be detected and simultaneously observed through the eyepiece.

Differential Interference Contrast (DIC). For acquisition of transmittance images, we used contrast-improving DIC optics. Interference by polarized light is divided by the first and recombined by the second Nomarski prism geometrically situated in the light path. In theory, the degree of contrast enhancement obtained depends on the relative differences in refractive indices within the sample and the surrounding medium, which are large in the case of hemozoin versus the red cells we image in this work.

Preparation of Samples for Microscopy. Aliquots (500 μL) of the culture were pelleted by washing in 10 volumes of incomplete medium at 2500 rpm for 5 min, resuspended in 100 μL of the same medium, and placed on No. 1 glass coverslips coated with poly-L-lysine (Sigma-Aldrich, P 8920). They were incubated for 5 min under a standard cell culture atmosphere (5% O_2/5% CO_2/90% N_2). Nonadherent cells were then gently washed off, and coverslips were sandwiched in specially designed chambers (see ref *4* and references therein). Typically, data acquisition for a given sample required approximately 25 min from initial removal of the cells from the T25 culture flask.

Data Acquisition. DIC data were typically collected using a Nikon 60× NA 1.4 oil objective with type A immersion oil ($n = 1.515$), an additional 1.5× intermediate magnification lens, a halogen lamp for transmittance illumination, a fixed 50 μm pinhole, a LP520 filter for transmittance filtering, and standard Perkin-Elmer Imaging Suite software for initial image acquisition. *z* spacing was set to 0.2 μm, appropriate for deconvolution; the exposure time was 100 ms, and the shear angle was 45°. We focused transmittance until Hz within the living parasite DV was clearly visible and presented the largest diameter possible. This put the initially defined *z* axis focal plane well within the confines of the DV. Once found, this *z* axis position was defined as 0. We then acquired a series of DIC images in successive 0.20 μm *z* axis displacements as we scanned through the parasite from the −2.4 μm to +2.4 μm position. The field of view typically contained one to five cells and was limited to ≤25% (center quarter) of maximal, further reducing the collection time of the *z* stacks. Using a convenient MatLab script (not the Imaging Suite software), data sets were exported at a high rate as sets of 25 16-bit tiff images to a portable hard drive.

Data Processing (3D restoration, segmentation, and volume measurements). To sharpen DIC data, we used a Weiner linear deblurring algorithm, followed by empirical bead calibration of *z* axis resolution (axial smearing) as described in the Results. Restoration and volume measurements were conducted using the Imaris 4.2.0 software package from Bitplane. The *z* series of optical sections (*z*

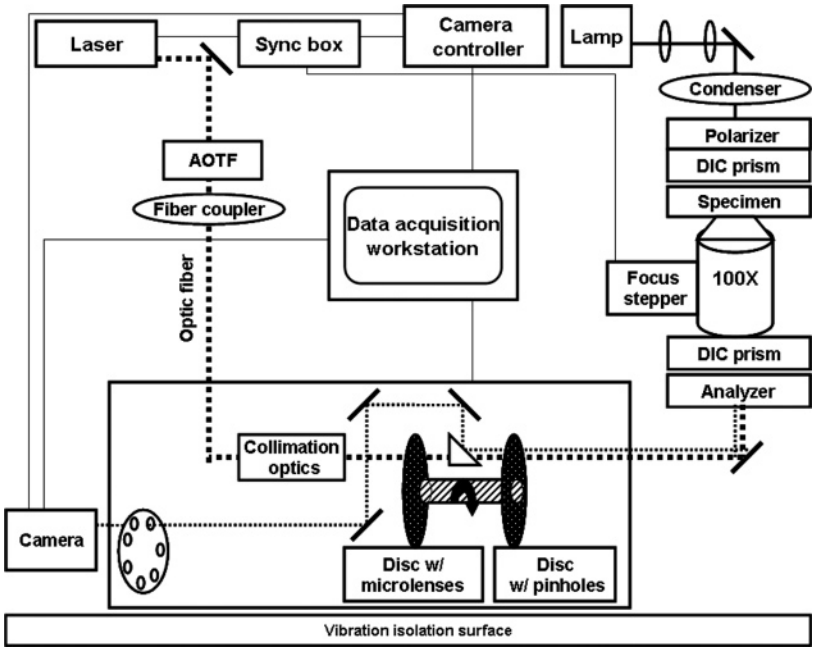

FIGURE 1: Schematic of the customized SDCM device used in this work. Note for DIC experiments (this paper) illumination of the sample follows the halogen lamp light path through the condenser, polarizer, and Wollaston prism to the specimen and then through the second prism, analyzer, spinning disk with pinholes, dichroic mirror, and emission filter to the camera. For fluorescence measurements (see ref *19*), light is from the laser through the AOTF (see Methods), fiber coupler, and then via an optic fiber through the collimation optics and both spinning disks, to the specimen. On the way to the camera, fluorescent light passes back through the disk pinholes, a dichroic mirror, and then again an emission filter in reaching the camera.

stacks) of the infected cells were imported into Imaris, sorted, and 3D rendered. After the average light intensity inside the RBC cytosol was calculated, image interference was subtracted, the practical range of the grayscale intensity was calculated, and the lower 60% of the signal was used as a segmentation cutoff value. Measurement of hemozoin volume was done by building an isosurface of the restored data set in Imaris and selecting Hz objects (defined by relative transmittance; see the Results). Data expressed as cubic micrometers per parasite DV were exported to Excel for further statistical analysis; data points are the average of ≥ 25 highly synchronized parasites $\pm$ the standard deviation in each case, unless otherwise noted.

RESULTS

Figure 1 is a schematic of the customized SDCM apparatus used in this work. Particularly important additions or modifications to the commercially available instrument are described in Methods. Notably, the Uniblitz high-speed shutter and the NEOS acousto-optic tunable filter provide excellent illumination control, and the 1.4 NA objective along with customized Nikon DIC optics provides adequate resolution for Hz quantification via transmittance experiments (see below). A variety of measurements using calibration beads and other standards in various media document the impressive time and spatial *x*, *y*, and *z* resolution of this customized instrument; we present some of these data below and in ref *19*. We note DIC experiments shown in this paper do not formally require the SDCM scanning head; however, we customized one apparatus that was versatile and that had both DIC and fluorescence data collection capabilities as shown here and in ref *19* (see the legend of Figure 1 for a description of the optical path).

Figure 2A shows representative Giemsa stains of the *P. falciparum* blood culture at different times after the third of three synchronization washes (see Methods), and Figure 2B quantifies parasite stages (defined visually as in Figure 2A) versus time. Like other reports, laboratory strains HB3 (CQS) and Dd2 (CQR) uniformly enter the early trophozoite stage 15 h after the third of three synchronization washes. Using these data as our guide, we obtained DIC SDCM *z* stacks

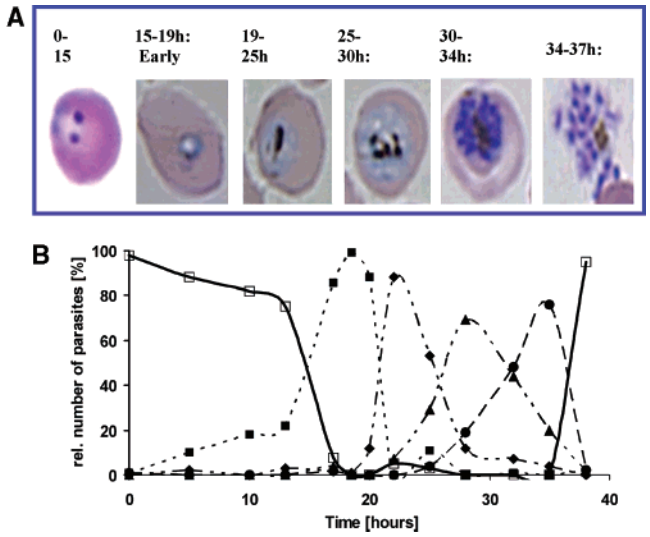

FIGURE 2: Results of the triple synchronization procedure used in this work. Panel A shows representative Giemsa-stained parasites at different times after the third synchronization wash. From left to right, the panels show ring, early, mid, and late trophozoite, schizont, and merozoite stages. Panel B plots counts of smears at different times for a synchronized *P. falciparum* culture stained with Giemsa dye. The culture used was tightly synchronized with 5% sorbitol: 4 and 14 h after first observed invasion in the preceding cycle and then 4 h after the first observed invasion in the presented cycle. At each of the time points, the stage of >100 parasites was determined and the relative number of the stages plotted: (□) rings, (■, ◆, and ▲) early, mid, and late trophozoites, respectively, and (●) schizonts.

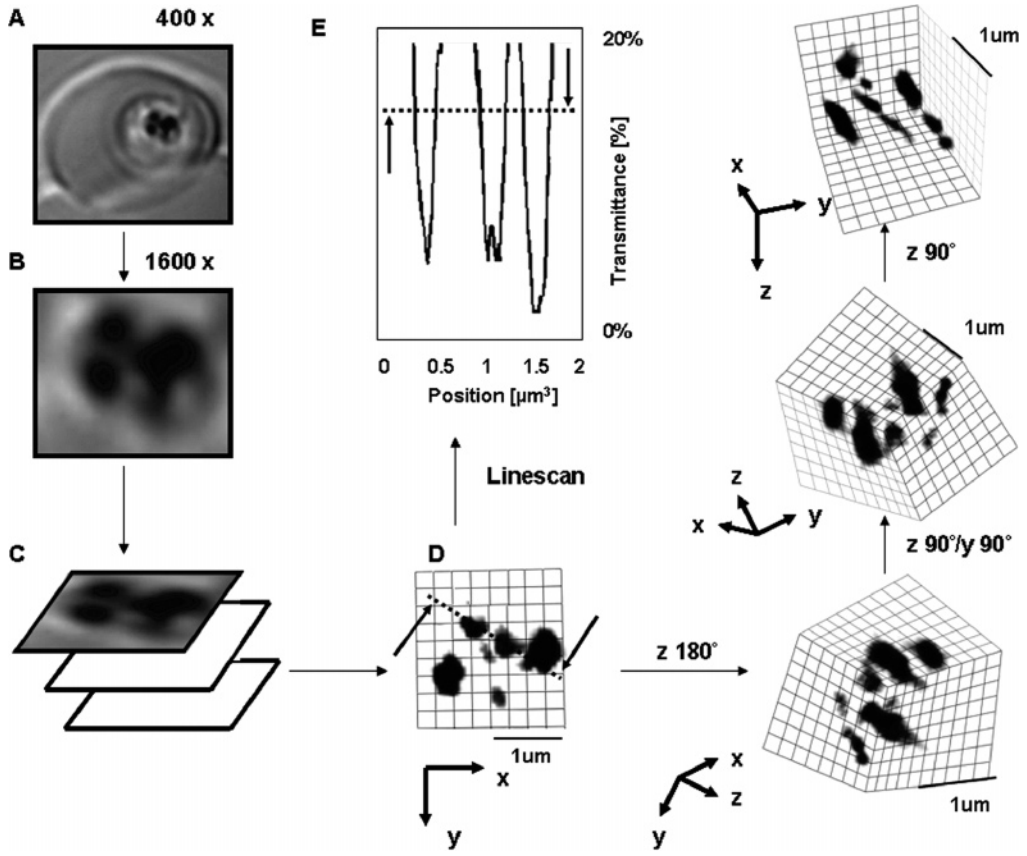

FIGURE 3: Illustration of data gathering and image rendering. Panels A−C represent acquistion and magnification of multiple *z* slices of DIC data (note ≥25 slices are actually obtained). Panel D shows a 2D projection of a single slice after deblurring (see the text), and panels to the right show 3D rendering of the full *z* stack after deblurring and correction for axial smearing. Panel E illustrates transmittance thresholding used to distinguish Hz particles. Note our measured *x*, *y*, and *z* dimensions of Hz crystal fragments are similar to those measured in serial electron microscopy images of sectioned DV (*9*).

for highly synchronized HB3 and Dd2 parasites at different stages of growth within the iRBC. Figure 3A−C illustrates how the data are collected to produce three-dimensional DIC data sets, and Figure 3D presents one representative data set for a late stage Dd2 trophozoite. Figure 3D (right-hand side) shows three frames that illustrate $\pi/2$ rotation of the full *z* stack of Hz DIC data about the *x*, *y*, and *z* axes. Three-dimensional renderings of these data (in Quicktime movie format) are available as Supporting Information. Figure 3E shows a plot of transmittance versus *x* axis position for one "*z* slice" within the data set shown schematically in Figure 3A−D. Since Hz is optically quite dense relative to all other material within the parasite cell, negative transmittance data with a 15% cutoff accurately define the Hz position in an individual slice. Each 3D data set for a living parasite is 25−30 *z* slices within the *x*−*y* plane (Figure 3A−D shows but one of these for clarity of illustration purposes). The cross-sectional surface area of Hz crystal fragments in an individual deblurred *z* slice (Figure 3D) can be quantified by counting pixels that measure <15% transmittance, since Hz is by far the most optically dense material in the cell. However, quantifying randomly distributed, nonuniform Hz fragments for the entire parasite DV requires a well-resolved, reconstructed, deblurred 3D *z* stack of images (shown in Figure 3D and panels to the right that are connected by arrows). Quantification also requires voxel analysis in place of histogram or pixel analysis.

Unfortunately, confocal optical microscopy produces *z* axis smearing in excess of the diffraction limit due to spherical aberration, discontinuities in the sample refractive index, and other issues. This is illustrated in Figure 4A, where an optically dense bead 0.80 μm in diameter is visualized via DIC SDCM using the same settings that were used to acquire the parasite images. The measured *x*−*y* diameter is quite close to the known diameter (see the scale bar at the top and bottom of the left-hand panels), but axial smearing increases the observed *x*−*z* diameter (top right panel) relative to known. This would lead to overestimation of Hz fragment volumes. To deblur and correct for inevitable *z* axis smearing of the parasite *z* stacks, we first applied a Weiner linear deconvolution algorithm (this proved superior to Hilbert and Sobel algorithms for these DIC data with their wide range of transmittance values; see the Discussion). Then, using similarly sharpened data sets for uniform bead size standards, we plotted known versus measured *x*−*z* values and computed the slope of this plot to derive an empirical correction factor (see Figure 4B). Applying the correction factor to the deblurred image yields *x* and *z* dimensions for the 0.80 μm diameter bead that are very close to known values (bottom right panel, Figure 4A). Combining these data processing steps with thresholding at a defined transmittance (e.g., Figure 3E) yields 3D versus time data for bead standards that give good agreement between known and measured *x*−*y* and *x*−*z* dimensions (Figure 4B, dashed lines, filled symbols) as well as calculated bead volumes (data not shown).

Following this image sharpening approach and the DIC SDCM voxel data analysis schematically illustrated in the right-hand side of Figure 3, we next calculated the total

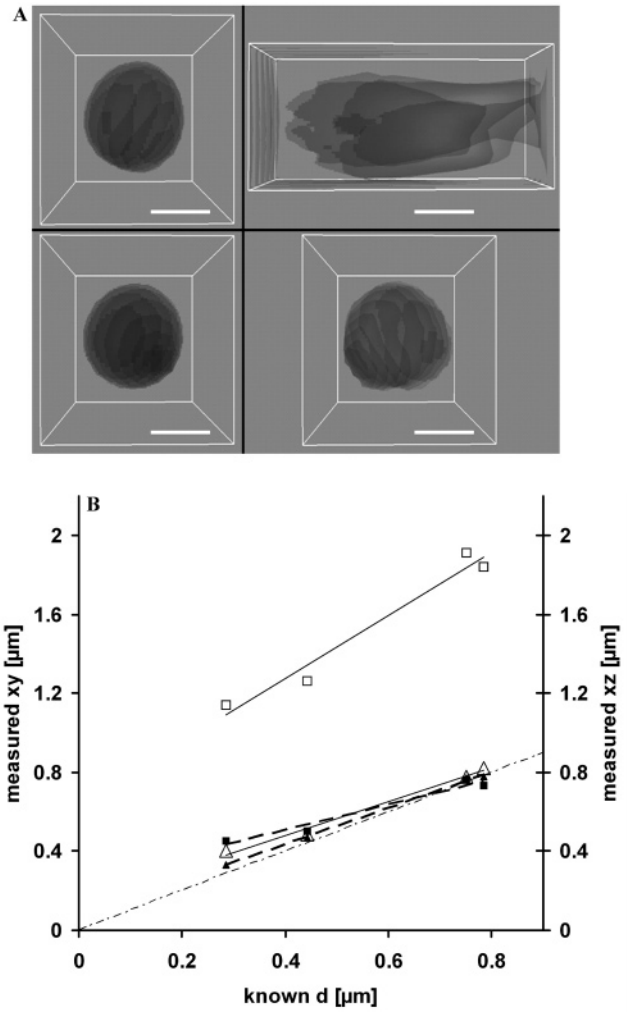

FIGURE 4: (A) Illustration of deblurring and axial smearing corrections. All four panels show an optically dense sphere 0.80 μm in diameter (known). The scale bar in each panel is 0.5 μm. The top and bottom left-hand-side panels show $x-y$ projection of the SDCM transmittance data for the bead before (top) and after (bottom) deblurring via the Wiener algorithm. The top right-hand-side panel shows the same raw data for the same bead but in the $x-z$ projection, and the bottom right panel is this $x-z$ projection after deblurring and correcting for axial smearing described in panel B. (B) We plotted measured $x-y$ (left y axis, △, solid line) or measured $x-z$ (right y axis, □, solid line) dimensions vs known diameter (x axis) for various size beads either before (empty symbols) or after (filled symbols, dashed lines) deblurring as described in the Results. Importantly, the raw $x-y$ or $x-z$ plots are linear before any deblurring procedure; thus, the axial smearing correction factor is essentially the inverse slope of the uncorrected $x-z$ line (□, solid line). The light dashed−dotted line shows the theoretical ideal, meaning the result that would be obtained for $x-y$ and $x-z$ lines if the deblurring procedure was perfect. Note that although the ideal is shown extended to the origin, rigorously, our Wiener deblurring/empirical bead standard approach does not likely produce perfectly linear results well below 250 nm (see the text and Discussion).

volume of Hz versus time for highly synchronized parasites growing within human RBC (Figure 5). Each point on these curves represents the average of ≥25 individual parasites. Time on the x axis refers to time after the last sorbitol synchronization wash (see Methods and Figure 2). Figure 5A overlays data for CQS and CQR laboratory strains HB3 and Dd2 wherein the CQR phenotype was created by drug selection, and Figure 5B shows similar data for CQS and CQR strains wherein the CQR phenotype was created by

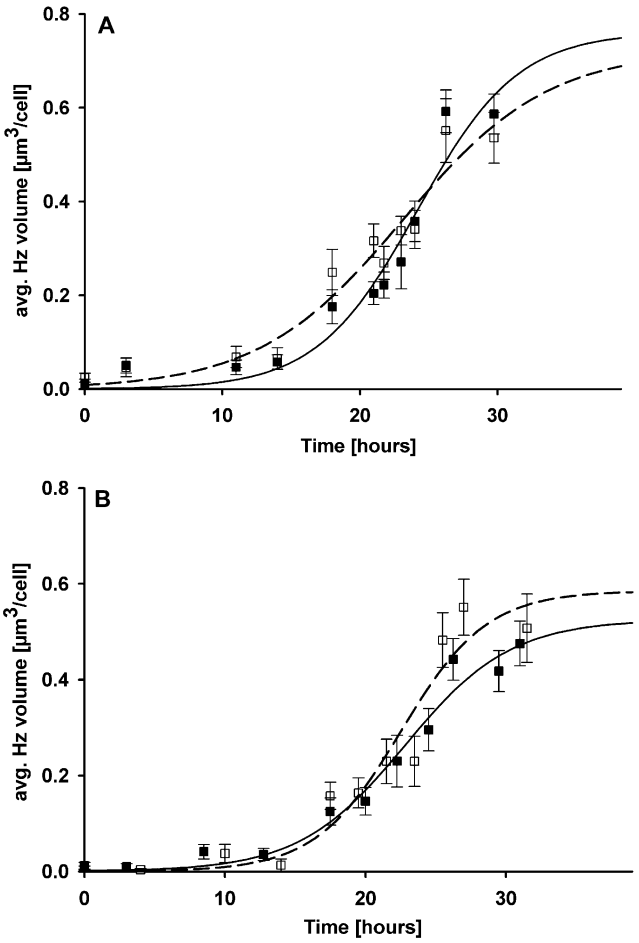

FIGURE 5: Rate of Hz production for CQR parasites Dd2 (top panel, ■) or C3Dd2 (bottom panel, ■) vs CQS parasites HB3 (top, □) or GC03 (bottom, □). Note the similar rates and extents of Hz formation for all four strains.

transfection with mutant *pfcrt* (*4* and references therein). The kinetics of Hz formation are found to be consistent with timing of the cell cycle as defined by visual inspection of Giemsa stains (Figure 2). Namely, for all four strains, appreciable Hz first appears between 15 and 19 h postsynchronization, corresponding to the early trophozoite stage at which conspicuous Hb degradation begins. Hz production then very rapidly proceeds and peaks between 25 and 27 h, corresponding to the late trophozoite−schizont boundary, where Hb proteolysis stops. Although similar conclusions could in theory be reached by tedious chemical extraction of Hz from bulk cultures, this is the first time that Hz formation kinetics have been directly quantified in vivo for living cells, and conveniently at the single-cell level.

Initial inspection of the Dd2 (CQR) versus HB3 (CQS) data (cf. Figure 5A) suggested to us that the kinetics of Hz formation might be slightly faster for the Dd2 strain, but this is not due to mutations in the PfCRT protein that are linked to CQR since a CQR strain created by transfection with mutant *pfcrt* [strain C3Dd2, Figure 5B (■)] does not exhibit the same effect when compared to the untransfected parent expressing wild-type PfCRT [strain GC03 (□)]. These results are significant since it has been suggested that the lower DV pH previously measured for CQR strains and linked to *pfcrt* mutations (*4*) might affect the relative rate of FPIX-to-Hz conversion (*26*; see also ref *11*). This proposal was based in part on in vitro data that clearly showed faster

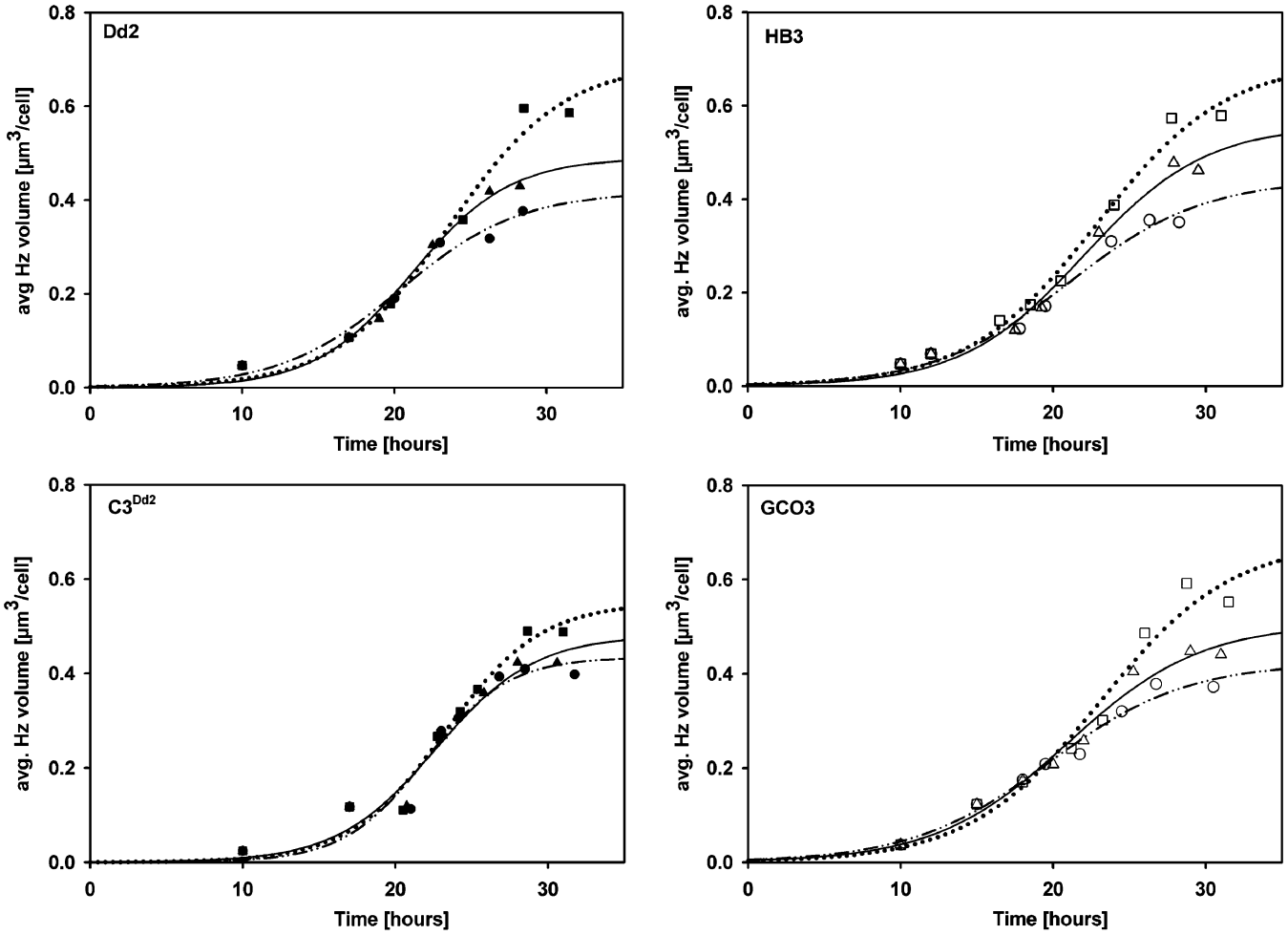

FIGURE 6: Rate of Hz production for the four strains shown in Figure 5, but in the absence (squares, top curve, each panel) vs the presence of chloroquine at either the IC_{50} for the strain or at $2IC_{50}$ (triangles, middle curve, and circles, bottom curve, respectively, for each panel). Each data set is fit by a sigmoidal curve. Hz production is similar for all strains at all doses of CQ until approximately 50% of Hz is formed, at which point Hz formation appears to plateau prematurely for all four strains in the presence of CQ, to a similar extent at a similar effective dose (see the text).

Hz formation at lower pH (*11*) as well as highly pH dependent heme aggregation (*26*). Therefore, either other characteristics of the DV for the CQR parasite negate the predicted acceleration of Hz formation at lower pH (e.g., see ref *19*), or release of free FPIX (and/or formation of tethered head-to-tail dimeric FPIX) is rate-limiting for Hz formation in vivo.

Figure 6A−D presents Hz formation versus time for the four strains in the absence and presence of CQ, wherein CQ [at concentrations corresponding to 0 (top curve), 1 (middle), and 2 (bottom) times the strain IC_{50}] is added at the ring−early trophozoite boundary. Thus, this experiment measures, in real time, how physiologically meaningful levels of CQ alter the production of Hz in vivo when the drug is administered at the time appreciable Hz synthesis begins. Again, although a variety of in vitro data show that CQ inhibits the formation of synthetic Hz from pure FPIX in a test tube (e.g., ref *11* and references therein), no direct kinetic quantification of this predicted in vivo effect has ever been presented.

Notably, we find that the apparent initial rate of Hz formation is not significantly affected by CQ for any strain. That is, from 15 to 22 h, during which time approximately 50% of total Hz is produced, the continuous presence of CQ at an even high dose (e.g., twice the IC_{50}) does not significantly affect net Hz production. Instead, CQ appears to prematurely truncate Hz production, reducing the steady state plateau normally achieved at 27−29 h. The reduction in net Hz production is clearly dose dependent and is similar for CQR and CQS strains assuming the effect of relative dose (relative IC_{50}) is examined, not absolute dose. If CQ at the IC_{50} for CQS strains is administered to CQR Dd2, no effect on Hz production is seen (data not shown).

We also tested whether high-dose CQ destabilizes preformed Hz in vivo. As Figure 7 clearly shows, even at a very high dose, CQ does not perceptibly reduce the volume of Hz present in the DV at the mid−late trophozoite boundry (25−27 h) for either CQR Dd2 parasites (top, solid bars) or CQS HB3 parasites (bottom, open bars). Thus, even very high levels of the drug do not measurably destabilize preformed Hz in the DV.

Since verapamil (VPL) is known to reverse CQR, we tested whether 1 μM VPL sensitized Dd2 parasites to Hz inhibition using a concentration of CQ that has no effect on its own for Dd2 (Figure 8). When 50 nM CQ is administered at the ring−trophozoite boundary in the absence of VPL, no Hz inhibition is observed for Dd2 (compare the first and second bars in Figure 8). However, when 1 μM VPL is included with 50 nM CQ (fourth bar), inhibition of Hz

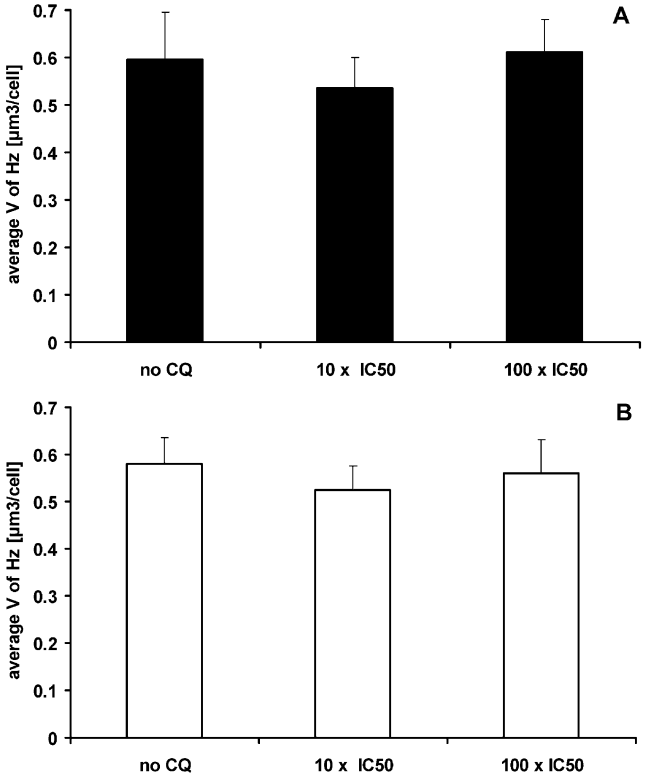

FIGURE 7: Effect of a 2 h pulse of CQ at either $10IC_{50}$ (middle) or $100IC_{50}$ (right-hand side) for CQR (A) or CQS (B) parasites. CQ at even very high doses does not destabilize preformed Hz in vivo.

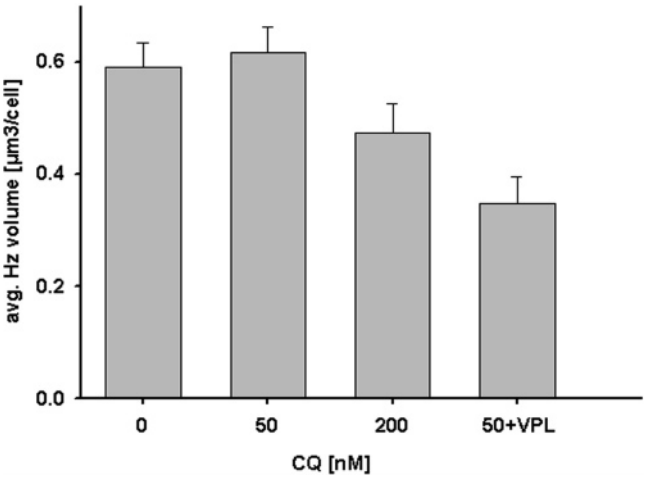

FIGURE 8: Inhibition of Hz formation with or without VPL for CQR Dd2 parasites (see the text). The first bar is Hz formation (at 27 h) in the absence of any drug, the second bar formation in the presence of 50 nM CQ (a dose that does not kill the Dd2 parasites), the third bar formation in the presence of 200 nM CQ (see also Figure 6), and the fourth bar formation in the presence of 50 nM CQ and 1 μM VPL.

formation similar to that seen at the IC_{50} dose of CQ alone (200 nM CQ, third bar Figure 8) is observed. Finally, we plotted percent inhibition of Hz formation versus growth inhibition under the same conditions for the different strains and conditions used in this study (Figure 9). A linear relationship was observed, supporting the notion that inhibition of Hz formation is the basis of CQ and CQ/VPL toxicities.

DISCUSSION

To our knowledge, no DIC studies that attempt to assemble 3D biochemical data versus time at the spatial resolution

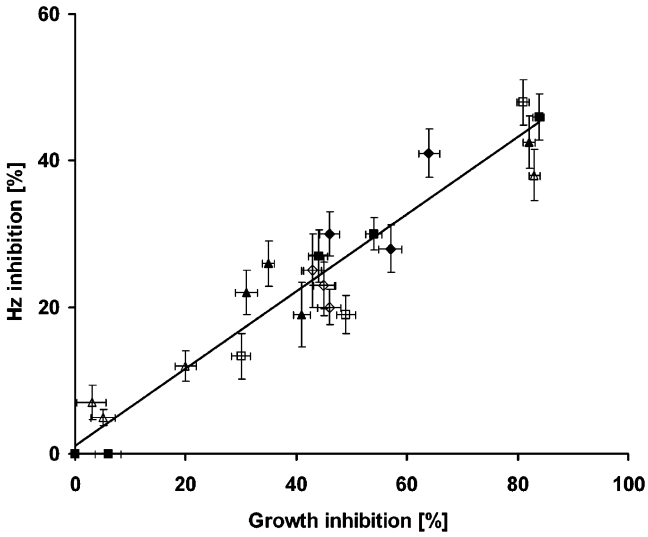

FIGURE 9: Linear relationship between percent inhibition of Hz formation vs percent growth inhibition as measured by parasitemia 25−30 h after addition of drug(s), for parasites treated as described in other sections of this paper. Filled squares show data for Dd2 parasites incubated with 0, 50, 100, 200, and 400 nM CQ (from left to right), empty squares data for HB3 incubated with 0, 10, 20, and 40 nM CQ (from left to right), filled triangles data for Dd2 incubated with 0, 0.25, 0.50, 1.0, and 10 μM VPL (from left to right), empty triangles data for HB3 incubated with 0, 0.25, 0.50, and 1.0 μM VPL (from left to right), filled diamonds data for Dd2 incubated with 50 nM CQ and either 0.25, 0.50, or 1.0 μM VPL (from left to right), and empty diamonds data for HB3 incubated with 20 nM CQ and either 0.25, 0.50, or 1.0 μM VPL. We find that VPL is more toxic to CQR parasites and that this is likely via a more potent effect on Hz inhibition.

presented in this paper have previously been published. The primary reason for this is that DIC is dependent upon differences in the refractive index of materials within cells, and although these vary (e.g., for DNA vs membranes, etc.), there are many regions within most cells where the gradient in refractive indices is modest or where large changes occur over distances well below the diffraction limit. Hence, resolution at the refractive index boundaries tends to be poor, even after application of advanced deblurring algorithms. However, importantly, few naturally occurring cellular components are as optically dense as Hz. Considerable Hz absorption is measured in these DIC experiments, which obviously contributes to the high quality of the images. That is, the observed contrast (DIC) is of high quality not only because Hz and its immediate surroundings have a different index of refraction relative to the surrounding RBC matrix but also because Hz absorbs light. In addition, Hz absorbs light quite efficiently over a broad range of wavelengths, which effectively eliminates complicated dispersion effects, allowing for more routine application of standard computational deblurring algorithms. The point is, in theory, high-resolution DIC images of red blood cells (naturally devoid of nuclei and other somewhat optically dense material) infected with mature malarial parasites should adequately visualize Hz production, assuming the data can be acquired in three dimensions at sufficient spatial and temporal resolution. But this has been a major challenge since malarial parasites wiggle and most conventional DIC systems are not outfitted to obtain *z* stacks in the time necessary to avoid significant blurring of Hz in the reconstructed image. In this paper, we present one approach that circumvents these

difficulties and allows the first direct quantification of Hz formation for living intraerythrocytic malarial parasites in situ. These data are collected in real time and at the single-cell level and have sufficient spatial resolution to precisely image Hz for living (moving) parasites. Via application of a standard deblurring algorithm and empirical calibration with beads with a known diameter, data are obtained near 200 nm resolution in the $x-y$ dimension with slightly lower (approximately 250 nm) resolution in the $x-z$ dimension. In general, these methods should be helpful in other applications that involve either contrast- or fluorescence-based imaging of moving objects and that require better than 250 nm 3D spatial and faster than 1 s temporal resolution (see also ref *19*).

Importantly, our method does not require large amounts of bulk culture. Quantifying Hz production at the resolution presented here, but using previously established methods, would require many liters of merozoite blood culture, followed by cell fractionation and chemical extraction. This can easily lead to underestimation of Hz due to loss of material during fractionation that involves multiple centrifugation steps, and/or inefficient dissolution and other problems inherent to various solvent extractions, as reviewed below. Alternatively, another previously established approach would be to obtain serial images by transmission electron microscopy followed by 3D reconstruction. This method could in principle provide sharper visual images of Hz relative to those we obtain here, but not necessarily better three-dimensional quantification of Hz volumes, because of inevitable perturbations caused by EM fixation methods and physically slicing the sample with a microtome knife. Moreover, the EM approach is enormously more tedious and time-consuming and does not offer a convenient way to analyze the effects of drugs, etc., versus time. In contrast, drugs, etc., can be easily introduced into the live culture during our measurements, in real time, via established perfusion methods (e.g., see refs *4* and *19*).

The kinetics of Hz formation we measure in vivo match the well-known visual criteria used to routinely identify stages of parasite differentiation. That is, as expected, the measured increase in Hz volume accelerates rapidly during the trophozoite stage and plateaus at the trophozoite−schizont boundary. The data are also somewhat consistent with previous studies that approximated Hz content at various stages of parasite development via cell fractionation and chemical extraction (e.g., see refs *27*−*29*), but differences between these studies and the present data should be noted. For example, a variety of estimates of how much FPIX is actually converted into Hz exist in the literature. These range from <30 to >90% of the available heme present within red cell hemoglobin. Data in ref *27* show approximately 5 μmol of FPIX in the Hz form is recovered from 10^{10} late stage trophozoites via cell fractionation and detergent extraction methods. Comparing this to the amount of Hb that is digested by the parasite suggests that only 40% of the heme released from Hb during digestion is recovered as Hz in this study. Another study (*28*) measures twice as much Hz using similar methods and reports approximately 90% inhibition of Hz formation by concentrations of CQ similar to those used here, when CQ is added during the ring stage of parasite development. Meshnick and colleagues (*29*) present data more similar to ours. They report amounts of Hz similar to the results of ref *28*, but a much milder inhibition of Hz formation at even higher dosages of CQ, relative to the results in ref *28*. There may well be CQ dose scheduling effects for Hz inhibition yet to uncover, meaning administration of CQ at different stages of the cell cycle yields significant differences in net Hz production. Future work using these more rapid and convenient SDCM methods should allow us to address the possibilities. In the previous extraction studies, the required cell culture volume makes analyzing many samples at different times or many different doses of CQ difficult, and as mentioned, fractionation of fragile intracellular parasites followed by extraction of Hz with detergent or other chemicals presents a number of additional challenges. However, none of these issues are a concern with the SDCM approach.

Using the unit cell dimensions of Hz published by Pagola et al. (*10*), we calculate that the volume of Hz we measure in vivo at the late trophozoite−schizont boundary plateau corresponds to 15 μmol per 10^{10} parasites. We measure that CQ at $2IC_{50}$ inhibits Hz formation by a relatively modest 30%, when added at the ring−trophozoite boundary, where Hz formation begins (see also ref *29*). Hz development in both CQS and CQR parasites is clearly inhibited by CQ, and to a similar extent at a similar relative dose (similar IC_{50}). Also, net toxicity (IC_{50}) is well correlated with net Hz inhibition in vivo for multiple strains and multiple doses (see also Figure 9), suggesting that inhibition of Hz formation is indeed the principle target of CQ.

In addition, we find fairly consistent production of Hz among four different strains, all of which plateau at approximately 0.6 μm^3/DV. In contrast, ref *27* measures approximately 2-fold differences (micromoles of heme as Hz per milligram of parasite protein) between strains. Large-scale comparison among many isolates and strains is feasible via the approach described here but is not feasible via the large-scale culturing and extraction approach. Thus, as more data are gathered, possible different levels of Hz among strains (and field isolates with various resistance and "fitness" phenotypes) can be resolved. It will also prove useful to analyze other *Plasmodium* species (e.g., *P. vivax*) that are currently impossible to conveniently culture.

We suggest that the kinetics of Hz formation in the presence of CQ are consistent with CQ having a much more significant effect at later stages of crystal growth, perhaps including interaction at the growing crystal face as suggested by Sullivan and colleagues (*30*). If CQ inhibited Hz formation in vivo only by irreversibly sequestering soluble noncrystalline FPIX, a more significant kinetic effect would be expected earlier, as suggested by comparison to in vitro data (e.g., ref *26* and references therein). In contrast, for all four strains that were examined, Hz production does not appear to be significantly affected in vivo until ~50% of Hz has been formed at a normal rate (i.e., the rate measured in the absence of drug). This suggests that, to a first approximation, initial nucleation proceeds at a similar rate in vivo with or without CQ. However, we note that mild effects on the kinetics of Hz production very early in trophozoite development cannot be ruled out. This is because young trophozoites might have a much larger proportion of very small (<150 nm long axis) Hz fragments, relative to what is seen for mid or late stage trophozoites. For mid−late stage trophozoites, the sporadic appearance of particu-

larly small fragments (sometimes revealed in electron microscopy data; cf. ref *9* and references therein) can in theory produce only an underestimation of Hz volume of 1−3% (B. C. Gligorijevic and P. D. Roepe, unpublished calculations). But if in very early trophozoites (14−15 h) the ratio of very small fragments to larger fragments is ≥1, limits in the resolution of our method could lead us to more significantly overestimate Hz volume (by measuring larger size for very small fragments) or underestimate it [by missing detection of some particularly small (<50 nm) fragments].

Regardless, since the unit cell dimensions of Hz crystals are known (*10*), and if we assume Hb digestion initially proceeds at a similar rate with or without CQ treatment (CQ is not known to inhibit the relevant proteases), then using a DV volume of 3.5 μm^3, we calculate that treatment with CQ at the IC_{50} dose could yield as much as 25 mM net uncrystallized FPIX. This is lower than might be expected on the basis of previous in vitro data but would be more than sufficient to promote significant cell damage. However, this is likely an overestimate of freely soluble FPIX that is present in the DV of a CQ-treated parasite. Most of the uncrystallized heme would not be in soluble form, since the combination of acidic DV pH and the presence of CQ would promote aggregation of all but a few micromoles (*26*). It is possible, on the basis of solubility data (*26*), that net freely soluble FPIX is at equal concentrations in the DV with or without CQ. If this is the case, then accumulated acid-aggregated FPIX species (noncrystalline FPIX or FPIX−CQ aggregates as described in ref *26*) could be the basis of CQ toxicity. How noncrystalline acid-aggregated heme might promote cell damage resulting in cell death is an important question yet to be explored. Regardless, the linear correlation observed when plotting in vivo Hz inhibition versus growth inhibition (Figure 9) strongly suggests that Hz inhibition and increased noncrystalline FPIX are the basis of CQ and CQ/VPL toxicity (see ref *31* for additional important data related to differential VPL toxicity). This is a simple, direct consequence of the Fitch hypothesis. It is tempting to extrapolate to include additional quinoline-based drugs, but since these have pK_a and other physicochemical properties different from those of CQ, formally, this requires further in vivo study. Also, we note that we have not eliminated the possibility that additional effects of CQ, concomitant with but chemically upstream of Hz formation, also contribute to CQ toxicity (e.g., traffic of Hb required for increased Hz production vs time).

Finally, by analyzing Giemsa staining up to 60 h after addition of CQ (data not shown), we note that regardless of the degree of Hz inhibition, every parasite treated with CQ at these doses proceeds from late stage trophozoite to a well-defined schizont. We also note that, as best as we can ascertain, the rate of this differentiation in the presence of drug appears to be indistinguishable from control, and a similar average number of newly formed merozoites are visible within the iRBC (data not shown). Parasitemia drops in the subsequent cell cycle, but in our hands (and via the benefit of our high-resolution single-cell visualization methods) other than decreased Hz production, CQ does not appear to significantly affect morphology or completion of the cell cycle during which CQ is initially administered. Thus, the toxic consequences of measured Hz inhibition are likely manifested during or immediately after schizogony. Perhaps membrane and/or oxidative damage caused by excess free FPIX or FPIX−drug conjugates affects the viability or infectivity of new merozoites. Alternatively, perhaps development of rings immediately after merozoite invasion is impaired. Further development of these high-speed imaging methods should allow us to address these and many other questions.

ACKNOWLEDGMENT

We thank D. Fidock (Albert Einstein College of Medicine, Bronx, NY) for cell lines $C3^{Dd2}$ and $C1^{GC03}$, T. Bennett (Georgetown University) for experimental help, and Drs. D. Sullivan (Johns Hopkins University, Baltimore, MD) and A. de Dios (Georgetown University) for helpful discussions.

SUPPORTING INFORMATION AVAILABLE

Quicktime movies that rotate data sets on the *x*, *y*, and *z* axes. This material is available free of charge via the Internet at http://pubs.acs.org.

REFERENCES

1. Plowe, C. V. (2005) Antimalarial drug resistance in Africa: Strategies for monitoring and deterrence, *Curr. Top. Microbiol. Immunol. 295*, 55−79.
2. Zhang, H., Howard, E. M., and Roepe, P. D. (2002) Analysis of the Antimalarial Drug Resistance Protein PfCRT Expressed in Yeast, *J. Biol. Chem. 277*, 49767−49775.
3. Gubbels, M. J., and Striepen, B. (2004) Studying the cell biology of apicomplexan parasites using fluorescent proteins, *Microsc. Microanal. 10* (5), 568−579.
4. Bennett, T. N., Kosar, A. D., Ursos, L. M. B., Dzekunov, S., Sidhu, A. B. S., Fidock, D. A., and Roepe, P. D. (2004) Drug resistance-associated PfCRT mutations confer decreased *Plasmodium falciparum* digestive vacuolar pH, *Mol. Biochem. Parasitol. 133*, 99−114.
5. Harrison, T., Samuel, B. U., Akompong, T., Hamm, H., Mohandas, N., Lomasney, J. W., and Haldar, K. (2003) Erythrocyte G protein-coupled receptor signaling in malarial infection, *Science 301* (5640), 1734−1736.
6. Rohrbach, P., Friedrich, O., Hentschel, J., Plattner, H., Fink, R. H., and Lanzer, M. (2005) Quantitative calcium measurements in subcellular compartments of *Plasmodium falciparum*-infected erythrocytes, *J. Biol. Chem. 280* (30), 27960−27969.
7. Chou, A. C., Chevli, R., and Fitch, C. D. (1980) Ferriprotoporphyrin IX fulfills the criteria for identification as the chloroquine receptor of malaria parasites, *Biochemistry 19* (8), 1543−1549.
8. Goldberg, D. E. (2005) in *Malaria: Drugs, Disease and Post-Genomic Biology* (Sullivan, D. J., and Krishna, S., Eds.) pp 275−292, Springer-Verlag, Heidelberg, Germany.
9. Scholl, P. F., Tripathi, A. K., and Sullivan, D. J. (2005) in *Malaria: Drugs, Disease and Post-Genomic Biology* (Sullivan, D. J., and Krishna, S., Eds.) pp 293−324, Springer-Verlag, Heidelberg, Germany.
10. Pagola, S., Stephens, P. W., Bohle, D. S., Kosar, A. D., and Madsen, S. K. (2000) The structure of malaria pigment β-haematin, *Nature 404*, 307−310.
11. Dorn, A., Vippagunta, S. R., Matile, H., Jaquet, C., Vennerstrom, J. L., and Ridley, R. G. (1998) An Assessment of Drug-Haematin Binding as a Mechanism for Inhibition of Haematin Polymerisation by Quinoline Antimalarials, *Biochem. Pharmacol. 55*, 727−736.
12. Yayon, A., Vande Waa, J. A., Yayon, M., Geary, T., and Jensen, J. B. (1983) Stage Dependent Effects of Chloroquine on *Plasmodium falciparum* in Vitro, *J. Protozool. 30* (4), 642−647.
13. Kuile, F. T., White, N. J., Holloway, P., Pasvol, G., and Krishna, S. (1993) *Plasmodium falciparum*: In Vitro Studies of the Pharmacodynamic Properties of Drugs Used for the Treatment of Severe Malaria, *Exp. Parasitol. 76*, 85−95.
14. Orjih, A. U. (1997) Heme Polymerase Activity and the Stage Specificity of Antimalarial Action of Chloroquine, *J. Pharmacol. Exp. Ther. 282*, 108−112.

15. Zarchin, S., Krugliak, M., and Ginsburg, H. (1986) Digestion fo the Host Erythroctye by Malaria Parasites is the Primary Target for Quinoline-Containing Antimalarials, *Biochem. Pharmacol. 35*, 2435−2442.
16. Leed, A., DuBay, K., Ursos, L. M. B., Sears, D., de Dios, A. C., and Roepe, P. D. (2002) Solution Structures of Antimalarial Drug/Heme Complexes, *Biochemistry 41*, 10245−10255.
17. de Dios, A. C., Cassabianca, L., Kosar, A., and Roepe, P. D. (2004) Structure of the Amodiaquine−FPIX μ oxo Dimer Solution Complex at Atomic Resolution, *Inorg. Chem. 43* (25), 8078−8084.
18. de Dios, A. C., Tycko, R., Ursos, L. M. B., and Roepe, P. D. (2003) NMR Studies of Chloroquine−Ferriprotoporphyrin IX Complex, *J. Phys. Chem. A 107*, 5821−5825.
19. Gligorijevic, B., Bennett, T., McAllister, R., Urbach, J. S., and Roepe, P. D. (2006) Spinning Disk Confocal Microscopy of Live, Intraerythrocytic Malarial Parasites. 2. Altered Vacuolar Volume Regulation in Drug Resistant Malaria, *Biochemistry 45*, pp 12411−12423.
20. Trager, W., and Jensen, J. B. (1976) Human malaria parasites in continuous culture, *Science 193*, 673−675.
21. Lambros, C., and Vanderberg, J. P. (1979) Synchronization of *Plasmodium falciparum* erythrocytic stages in culture, *J. Parasitol. 65* (3), 418−420.
22. Nakano, A. (2002) Spinning disk confocal microscopy: Cutting edge tool for imaging of membrane traffic, *Cell Struct. Funct. 27*, 349−355.
23. Mellors, R. C., and Silver, R. (1951) A microfluorometric scanner for the differential detection of cells: Application to exfoliative cytology, *Science 114*, 356−360.
24. Tanami, T., Otsuki, S., Tomosada, N., Kosugi, Y., Shimizu, M., and Ishida, H. (2002) High-speed 1-frame/ms scanning confocal microscope with a microlens and Nipkow disks, *Appl. Opt. 41* (22), 4704−4708.
25. Inoue, S., and Spring, K. R. (1997) *Video Microscopy*, 2nd ed., Plenum Press, New York.
26. Ursos, L. M. B., DuBay, K. F., and Roepe, P. D. (2001) Antimalarial Drugs Influence the pH Dependent Solubility of Heme via Apparent Nucleation Phenomena, *Mol. Biochem. Parasitol. 112*, 11−17.
27. Zhang, J., Krugliak, M., and Ginsburg, H. (1999) The fate of ferriprotorphyrin IX in malaria infected erythrocytes in conjunction with the mode of action of antimalarial drugs, *Mol. Biochem. Parasitol. 99* (1), 129−141.
28. Orjih, A. U., Ryerse, J. S., and Fitch, C. D. (1994) Hemoglobin catabolism and the killing of intraerythrocytic *plasmodium falciparum* by chloroquine, *Experientia 50*, 34−39.
29. Asawamahasakda, W., Ittarat, I., Chang, C.-C., McElroy, P., and Meshnick, S. R. (1994) *Mol. Biochem. Parasitol. 67*, 183−191.
30. Chong, C. R., and Sullivan, D. J. (2003) *Biochem. Pharmacol. 66*, 2201−2212.
31. Martiney, J. A., Cerami, A., and Slater, A. F. (1995) Verapamil Reversal of Chloroquine Resistance in the Malaria Parasite *Plasmodium falciparum* Is Specific for Resistant Parasites and Independent of the Weak Base Effect, *J. Biol. Chem. 270* (38), 22393−22398.

BI061033F